Kyle Hughes[1]
Department of Mechanical and Aerospace Engineering, University of Florida, Gainesville, FL 32611
e-mail: kylethughes89@ufl.edu

S. Balachandar
Professor
Department of Mechanical and Aerospace Engineering, University of Florida, Gainesville, FL 32611

Nam H. Kim
Professor
Department of Mechanical and Aerospace Engineering, University of Florida, Gainesville, FL 32611

Chanyoung Park
Department of Mechanical and Aerospace Engineering, University of Florida, Gainesville, FL 32611

Raphael Haftka
Professor
Department of Mechanical and Aerospace Engineering, University of Florida, Gainesville, FL 32611

Angela Diggs
Air Force Research Laboratory, Eglin Air Force Base, FL 32542

Donald M. Littrell
Air Force Research Laboratory, Eglin Air Force Base, FL 32542

Jason Darr
Air Force Research Laboratory, Eglin Air Force Base, FL 32542

Forensic Uncertainty Quantification for Experiments on the Explosively Driven Motion of Particles

Six explosive experiments were performed in October 2014 and February of 2015 at the Munitions Directorate of the Air Force Research Laboratory with the goal of providing validation-quality data for particle drag models in the extreme regime of detonation. Three repeated single particle experiments and three particle array experiments were conducted. The time-varying position of the particles was captured within the explosive products by X-ray imaging. The contact front and shock locations were captured by high-speed photography to provide information on the early time gas behavior. Since these experiments were performed in the past and could not be repeated, we faced an interesting challenge of quantifying and reducing uncertainty through a detailed investigation of the experimental setup and operating conditions. This paper presents the results from these unique experiments, which can serve as benchmark for future modeling, and also our effort to reduce uncertainty, which we dub forensic uncertainty quantification (FUQ).
[DOI: 10.1115/1.4043478]

1 Introduction

With the expected rigor of uncertainty quantification (UQ) increasing with time, it is often desirable to go back to past experiments and redo the UQ to meet more modern standards. This may permit uncertainty reduction, which will make the experiments more useful in many ways including serving as benchmark for evaluation of physical models and validation of simulation. It must be stressed that performing new experiments that build upon the lessons learned from the past experiments may be the ideal option in terms of uncertainty reduction. However, under situations when repeating the past experiments is not an option for varying financial, political, or other reasons, it is imperative that we go back and investigate the relevant past experiments in greater detail.

This paper reports on a set of experiments performed in October 2014 and February of 2015 at the Munitions Directorate of the Air Force Research Laboratory at the Eglin Air Force Base. Careful measurements were taken of the impulsive motion imparted on spherical metal particles by explosive detonation. The intent of the experiments was to provide valuable information on the momentum transferred to particles from the surrounding gas under conditions of extreme pressure, density, and temperature. Typically, the momentum transfer between a particle and the surrounding fluid is modeled in terms of drag and lift forces on the particle.

In particular, empirical drag correlations have been advanced in the past to cover a wide range of Reynolds and Mach numbers that are based on particle diameter and relative velocity [1–3]. In the incompressible and high-speed regimes, these empirical correlations were developed and tested using wind tunnel, shock-tube, and ballistic experiments, wherein the particle motion was measured as a function of time [4–6]. From accurate time-resolved measurements of particle position, and gas velocity around the particle, it was possible for later researchers to develop appropriate drag models that best fit the experimental data.

[1]Corresponding author.

Manuscript received June 21, 2018; final manuscript received April 5, 2019; published online May 13, 2019. Assoc. Editor: Kyle Daun.

The main purpose of the experimental measurements to be reported here is to provide similar information on particle motion versus time under explosive conditions. Since such data are currently lacking, the present results are intended to fill a gap in our knowledge. Detailed measurements under detonation conditions are difficult, due to extreme pressures and temperatures. However, accurate measurements with minimal uncertainty are needed for the data to be useful in developing and testing drag laws that are appropriate under explosive conditions. Thus, an important focus of the paper is to report on our rigorous efforts toward uncertainty reduction.

Since the experiments were performed in the past and could not be repeated, we faced an interesting challenge of quantifying and reducing uncertainty through a detailed investigation of the experimental setup and operating conditions. This paper reports on our effort, which we dub forensic uncertainty quantification (FUQ) because of its similarity to crime scene forensic investigation. Finally, it should be pointed out that the unique results from the present experiments on impulsive particle motion resulting from a detonation can be of value as a benchmark against which future simulation results can be validated.

In this paper, the FUQ analogy will be briefly presented in Sec. 2. Its application to explosively driven particle experiments of interest is detailed next in Sec. 3. Section 4 will present the findings of the investigation with regards to the uncertain inputs. A summary table is presented at the end of the section (see Table 8). Finally, the experimental results will be presented in Sec. 5. Details of processing the data to obtain the shock time of arrival, the particle position, the contact front location, and the transverse shock location will be presented. Section 6 will present an overall summary of findings from the investigation.

2 Forensic Uncertainty Quantification

Forensic uncertainty quantification is the investigation of old experiments to upgrade and reduce the uncertainty estimates in inputs and measurements. The investigator carefully reconstructs details of the experimental setup, quantifies uncertain inputs, and provides meaningful data with associated uncertainty (see Fig. 1). The term "forensic" is used specifically here to invoke imagery of a crime scene investigation as a useful analogy when performing the investigation.

2.1 Forensic Investigator. Who should act as the forensic investigator? If time is the priority, the experimentalist has the most knowledge of the experiment prior to the investigation and may shorten the process significantly by serving as the forensic investigator. Additionally, the experimentalist may choose to act as the forensic investigator to update old experiments to meet the more stringent standards of UQ present today. However, whenever possible, it is recommended that the investigator be an independent third party who brings an unbiased perspective.

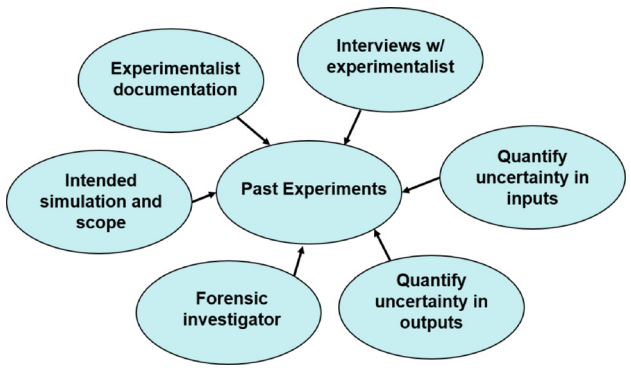

Fig. 1 Elements of FUQ. The goal of the investigation is to upgrade and reduce the uncertainty estimates in inputs and measurements.

An independent investigator lends credibility to the UQ and has sufficient time to carefully document all uncertainty sources. For the experiments presented here, the primary author (Hughes) was not initially involved with the experiments but was later tasked with performing UQ on the experiments.

2.2 Intended Scope. The investigator must carefully define the scope of the FUQ. What models will be validated? What inputs are critical to the model? What uncertainty sources could indirectly affect the data? In the current experiments, the focus is on the particle drag model under extreme conditions. The investigation may reasonably limit the scope of the work to exclude additional physics. For instance, no effort was expended in measuring or quantifying heat transfer and related quantities, since they do not directly influence the drag model.

2.3 "Crime Scene" Documentation. Documentation may be considered any files that are not raw data. For our case, the experimental documentation took a variety of forms including a shot log with details of the experimental shots, internal PowerPoint slide presentations, a written summary document, part drawings, and photographs of the experimental setup. Of these, the experimental shot log and photographs have been of the most value.

2.4 "Witness" Interviews. The documentation mentioned above must be examined and corroborated with the help of the experimentalist. For our case, the actual loading of the particles with respect to the explosive did not match the engineering drawings of the setup. The experimentalist was able to provide their recollection of what was done during the test. Conversely, their recollection may also be flawed. Photographic evidence proved the existence of a test configuration not remembered being used by the experimentalist.

2.5 "Forensics Laboratory". The experimental setup is often disassembled or otherwise inaccessible. Laboratory tests may then be used to attempt to recreate and measure key aspects of the experiment. In this paper, uncertain inputs have been quantified through testing of representative samples. For example, in the gathered documentation, only the nominal size and material of the particles were reported. This level of detail was deemed as insufficient as particle parameters are critical for simulations. Upon request, the experimentalists provided a representative sample of the particles that were tested in the laboratory.

3 Microscale Explosive Dispersal of Particles

First, the role of each author will be discussed. Second, the experimental motivation is presented to define the scope. Third, the reconstruction of the experimental setup is detailed. Finally, this section will be concluded with some notes on the forensic investigation.

3.1 Role of Authors. To provide transparency to the forensic investigation, the role of each author is discussed in brief here. The first author, Hughes, played the role of forensic investigator under the guidance of authors Kim, Haftka, and Park. Balachandar and Diggs helped to define the intended scope and provided guidance on identifying critical inputs. Diggs was also instrumental in locating representative samples for testing and analysis. Littrell designed and supervised the experiments while Darr executed the tests. Littrell and Darr acted as primary witnesses providing Hughes with all available data and documentation while also collaborating with the authors to establish the details of the experimental setup.

3.2 Experiment Motivation and Investigation Scope. The experiments under consideration were performed for obtaining validation-quality data on the particle motion under detonation conditions. The motivation for the experiments is of critical

importance when performing the forensic uncertainty quantification because it helps to define the scope of the investigation [7].

3.2.1 Background. Consider a problem where an array of spherical particles is emplaced on the flat end of a cylindrical charge of energetic material. At the end of the complete detonation, the energetic material is replaced by the highly compressed gaseous products of detonation at very high temperature and pressure, whose density initially is comparable to that of the original condensed-phase energetic material. As the hot, compressed products of detonation expands into the surrounding medium, a strong air shock forms and propagates over the array of particles. The shock is followed by an intense contact discontinuity between the products of detonation and the surrounding air. Initially, the density jump across this contact discontinuity is very large and it too propagates over the array of particles.

The shock and the contact discontinuity impart momentum to the particles and set them in rapid motion. The initial rapid momentum exchange is through inviscid mechanisms and occurs on the acoustic time scale. The acoustic time scale is the time over which the shock traverses the particle radius, R_p/u_s, where R_p is the radius of the particle and u_s is the shock speed. Due to this near-impulsive acceleration, the particles reach a substantial fraction of the postshock gas velocity on the order of the acoustic time scale [8,9]. Subsequently, viscous mechanisms continue to transfer momentum and the particles accelerate to the postshock gas velocity. Due to volumetric expansion, the postshock gas velocity continues to decrease over time, so eventually the particle velocity exceeds the gas velocity and then the momentum exchange tends to slow the particles.

Here, results are presented from experiments where the focus is to quantify the very early periods of this complex momentum transfer process. Thus, the primary focus is on the inviscid mechanisms of momentum transfer as the shock and the contact discontinuity pass through the bed of particles. Even in the limit of an isolated particle, only recently are researchers beginning to understand and accurately model shock propagation over a particle. High-quality experiments of shock propagation over an isolated particle in a shock tube have been performed with innovative methods to accurately measure the rapidly varying force on the particle. Experiments by Takayama and coworkers [10–12] used an accelerometer installed inside the sphere to measure the force on the particle at submicrosecond resolution, while Bredin and Skews [13] used a stress-wave drag balance to measure the time-dependent force on a stationary particle positioned within the shock tube.

All these experiments measured the peak force on the particle to be more than an order of magnitude greater than what is predicted by conventional quasi-steady drag force model. In addition, the experimentalists observed the peak force to occur as the shock wave traverses the particle. The long time force on the particle, where the shock is well downstream of the particle, is observed to be well predicted by the conventional quasi-steady drag force model using the relative velocity between the particle and the postshock gas [14]. Furthermore, it is observed that the transition from the peak force to the steady-state force can be nonmonotonic. Most curiously, shortly after the shock propagation, the force on the particle is directed in the direction opposite to the direction of postshock gas flow, which is due to the shock wave diffraction around the sphere and refocusing on the backside of the sphere [14]. There have also been shock tube and high-speed flow experiments where a single particle or a small collection of particles are allowed to move freely in response to forces exerted on them by the shock and the postshock flow [6,15–17]. In these experiments, a detailed time history of the particle motion allows the aerodynamic force on them to be extracted. However, the focus was mainly on their long term quasi-steady force and not on the early inviscid contribution.

3.2.2 Current Focus. The above shock-tube experiments differ from the present problem of particle interaction with a postdetonation flow in two significant ways:

(1) In the shock tube experiments, the particle location was sufficiently downstream from the initial interface between high and low pressure sections that only the interaction of the shock with the particle was considered, while in the case of postdetonation flow, the particle is first subjected to the shock, which is quickly followed by the contact discontinuity.
(2) In the above-mentioned shock tube experiments, the shock Mach number was limited so that the Mach number of the postshock uniform flow was below the critical value of 0.6. Whereas, as the detonation propagates into the ambient as an air shock, the initial value of the shock Mach number can be very large (in excess of 10 or more). Although the shock and the intensity of the flow behind the shock rapidly decays as the flow expands radially out, initially, the Mach number of the postshock flow remains sufficiently above critical. As a result, shocklets form around the particle, which coalesce to form a standing bow shock as the Mach number of the postshock flow becomes supersonic.

Due to the high speeds and optical opacity of the explosive products, detailed experimental investigations of explosively driven particles are far more challenging. Frost and coworkers [18–21] have conducted a series of experiments under varying test configurations to understand the nature of explosive dispersal of particles and the resulting instabilities of the rapidly advancing particle front through high-speed video analysis. However, these have mainly focused on the collective behavior of a very large number of small particles and their interaction with the shock and the high-speed detonation products. The current experiments are aimed at bridging the experimental gap that exists between highly resolved measurements of an isolated or small collection of particles in the modest Mach number regime of a shock tube and the high-speed imaging of an explosive dispersal of particles.

There is very little experimental information currently available that accurately documents the motion of a particle subjected to an explosively driven shock wave followed by a contact. Such information is essential to validate new force expressions that have been proposed as compressible generalizations of the Maxey–Riley–Gatignol equation [22,23] and thus can be applied to cases of shock–particle interaction [24–26]. By comparing the results against shock-tube laboratory experiments [10,13] it has been shown that the generalized force formula captures the nonmonotonic force evolution quite accurately; especially, the magnitude and the timing of the peak force are very well predicted. The purpose here is to provide detailed measurements of the particle motion under detonation conditions, to facilitate the development of appropriate drag models.

For the current study, particles are placed on the flat ends of a cylindrical charge. Detonation is initiated at the other end of the cylindrical charge and upon completion of the detonation process, the particle array is subjected to a reasonably flat air shock. X-ray images provide detailed measurement of the particle location in the near field immediately following the completion of detonation. The X-ray penetrates through the dense cloud of detonation products and allows for the identification of the metal particles. A time sequence of X-ray images is used to obtain the particle trajectory. The experiments consider isolated and well-defined arrays of O(10) particles so that the effect of their interaction on particle motion can be ascertained.

3.3 Experimental Setup. Two sets of experiments were performed at Eglin Air Force Base (Eglin AFB). Experimental details have been reconstructed from correspondence with Eglin AFB personnel, photographs of the setup, and experiment documentation. Note that all photographs of the experimental setup presented here were taken at the time of the tests.

An initial set of three experiments was performed in October 2014 and then a follow-on series of three tests in February 2015. A total of six explosive tests will be discussed. Due to

improvements in instrumentation between the two sets of tests, the two setups are distinct and so care will be taken to underscore the differences. Furthermore, the set to which the test belongs will be indicated in the identifier, e.g., Feb15-1 indicates that it is the first test in the February 2015 set. In addition, the loading configuration of the particles with respect to the explosive and the casing is not consistent across all tests. Three distinct configurations were used. A summary of the tests is shown in Table 1 with the identifier, the particle configuration, and the loading configuration.

In all tests, the particles were 2-mm diameter tungsten spheres. The particles were highly spherical. Repeated measurements by the forensic investigator of the particle diameter with a micrometer produced variability within the uncertainty of the micrometer. The particles were driven by three stacked pellets of PBXN-5 explosive, each nominally 12.7-mm long with 12.7-mm diameter, and initiated by a Teledyne RISI RP-83 detonator. PBXN-5 was chosen as the explosive for the extensive characterization readily available in the literature [27].

The explosives were contained within a steel cylinder with a 50.4-mm outer diameter and a 13.0-mm bore. The bore was made slightly larger than the explosive to allow easy loading of the explosive pellets. Figure 2 details the three different configurations used to mount the particles on the explosive. Figure 2(*a*) shows a detailed cross section of the test article.

The configuration used for each test is specified in Table 1. Figure 2(*a*) shows configuration 1 where the explosive was flush with the back step of the casing, placing the particle within a short barrel. In configuration 2, shown in Fig. 2(*c*), the particles were initially mounted on a small plastic holder, that holder was placed flush with the end of the explosive casing, and the explosive advanced to be in contact with the particles. Figure 2(*e*) shows configuration 3 where the particles were mounted on tape and then mounted on the explosive casing. The explosive is then advanced to be in contact with the particles. Note that configuration 3 in Fig. 2(*e*) was not provided by the experimentalist and only discovered as a result of the forensic investigation.

The front view of the particle assemblies is available in Fig. 3. In all tests, apart from the four-particle test, the particles were placed on a small plastic holder before being mounted on the explosive casing. The holder allowed reasonable confidence in the initial location of the particles and their initial spacing. The holder is slightly smaller diameter than the casing, biasing the initial locations at most 0.25 mm in the particle plane. The plastic holders were not observed in the X-ray images and it may be reasonably assumed that the holders were destroyed during the explosive event. No plastic fragments were recovered after the testing.

The first experimental setup, Oct14, is shown below in Fig. 4. Pressure traces were collected with two PCB® Piezotronics Model 137A23 pressure probes sampled at 10 MHz oriented toward the initial location of the particles. High-speed imagery was collected with a specialized imaging SIMACON coupled to a xenon flash lamp and sampled at 333 kHz with a resolution of 1260×940. However, hardware limitations prevent more than 16 images from being collected from the SIMACON per test. The Phantom v611 field of view was placed approximately 23 cm downstream from the test article and sampled at 91 kHz with a resolution of 512×28 with light provided by a light-emitting diode (LED) flash lamp. Above the test article three Hewlett-Packard 150 keV X-ray heads oriented toward the test article. An accompanying X-ray film was located below the test article. The times at which the X-ray heads were triggered were recorded using a Rogowski coil. Digital oscilloscope records of the trigger signals were recorded at 10 MHz.

Table 1 Number of particles and test configuration for Eglin AFB experiments. Configurations are detailed in Fig. 2.

Test #	Particle(s)	Configuration
Oct14-1	Single	1
Oct14-2	Ring of 7	2
Oct14-3	4×4 Grid (16 total)	2
Feb15-1	Single	2
Feb15-2	Single	2
Feb15-3	Diamond (4 total)	3

The experimental setup for the seconds set of tests, Feb15, included additional diagnostics such as a fourth X-ray head, six more pressure probes, and an additional near-field camera. The changes can be observed in Fig. 5. The eight pressure probes were arranged in a spherical grid placing each probe nominally 86 cm from the test article. Table 2 contains the nominal location of the pressure probes in Cartesian coordinates. The probe locations were confirmed with a tape measure before each test. The locations were therefore characterized with approximately 1% error. An aluminum witness panel, approximately 2 mm thick, is located 168 cm downstream of the test article.

The probes were PCB Model 137A23 pressure transducers and were sampled at 100 kHz. The Specialized Imaging SIMACON was sampled at 666 kHz with a resolution of 1260×940 with light provided by the xenon flash lamp. The Phantom v611 was sampled at 10 kHz with a resolution of 1280×480. The Phantom v611 again utilized the LED flash lamp as a light source. The additional camera was a Phantom Miro M310 with a Mega Flash PF300 flash bulb light source. A polarizing filter was placed between the flash bulb and the flow field and a second polarizer placed on the Miro M310 lenses in an effort to help image the shock and combustion waves (both polarizers were oriented in the same direction). The frame rates and resolutions for the Miro M310 are recorded in Table 3. Digital oscilloscope records of the trigger signals were recorded at 1 MHz. Casings were significantly fragmented during testing. A postshot picture of the casing is shown in Fig. 6.

3.4 Forensic Effort to Establish Experimental Setup. Details of the experimental setup were surprisingly difficult to establish, especially to the degree to make the results useful for drag model development or validation. While details such as camera-to-target distances were recorded, other details such as how exactly the particles were mounted was sparse. Furthermore, early assumptions made on some details of the experimental setup proved false on later investigation. For example:

(1) It was initially assumed that all the tests placed the explosive flush with the back step of the casing as in configuration 1 (Fig. 2(*a*)). It was thought that only the particles were advanced forward in the barrel. The available photographs showing only the front views prevented conclusions to the contrary.
(2) The plastic holders were not emphasized in the documentation and it was initially thought the particles were mounted only with tape. PBXN-5 is white in color and so the observed white material was thought to be the explosive.

Only when the experimentalists were presented with engineering drawings were they able to recall the finer details on how exactly the particles were mounted and correct the wrong assumptions. Conversely, the experimentalists insisted that plastic buttons had been used on all tests. However, examining the photograph in Fig. 2(*f*), it is observed that the departures from nominal location are too large if the particles were mounted using a holder. Additional photographs show the experimentalists mounting the particles on tape with no holder in view (indeed, these were the photographs that led to the assumption no holders were used in any tests). It was, therefore, concluded that the final test used a different configuration with no holder.

4 Forensic Uncertainty Quantification of Inputs

This section will demonstrate the application of forensic uncertainty quantification with regard to input parameters. The results

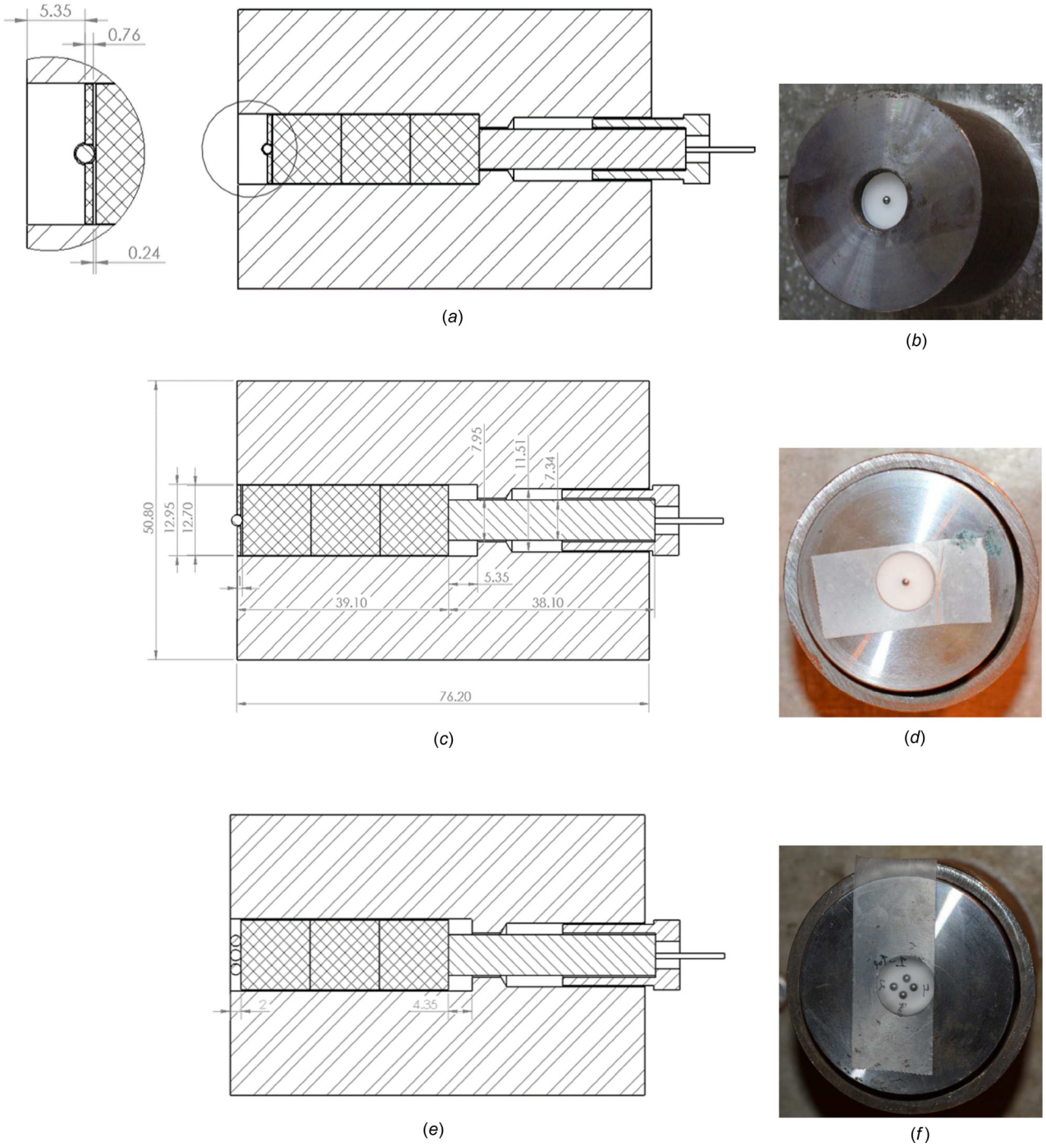

Fig. 2 Three distinct loading configurations were used to mount the particle assemblies on the explosive. Dimensions are in mm. (*a*) Configuration 1 cross section showing the explosive flush with the back-step. The particle is mounted on a plastic holder and then placed flush with the explosive. (*c*) Configuration 2 showing the particle holder flush with the end of casing and the explosive advanced to be in contact. (*e*) Configuration 3 shows that no plastic holder was used in this case but instead mounted on the tape and then placed flush on the end of the casing. (*b*), (*d*), and (*f*) photographic confirmation of the three configurations: (*b*) configuration 1, (*d*) configuration 2, and (*f*) configuration 3.

of testing representative samples to obtain their variability will be presented. Additional input uncertainty is obtained from image analysis of experimental setup photographs. A table is presented at the end of the section summarizing findings for each uncertain input.

4.1 Particle Diameter. A representative sample of 52 particles was provided by the experimentalists. While the particle manufacturer is unknown, the particles were drawn from the same batch as the experiments. The results of micrometer measurements are shown in the histogram in Fig. 7.

Fitting of the particle diameter distribution with 16 candidate distributions showed the two-parameter Weibull distribution (scale parameter of 2.019 and shape parameter of 321.9) with a minimum negative log likelihood. To test the goodness-of-fit for the Weibull distribution, the Lilliefors test was performed with 95% confidence and rejected with a p-value of 3.18×10^{-5}. The

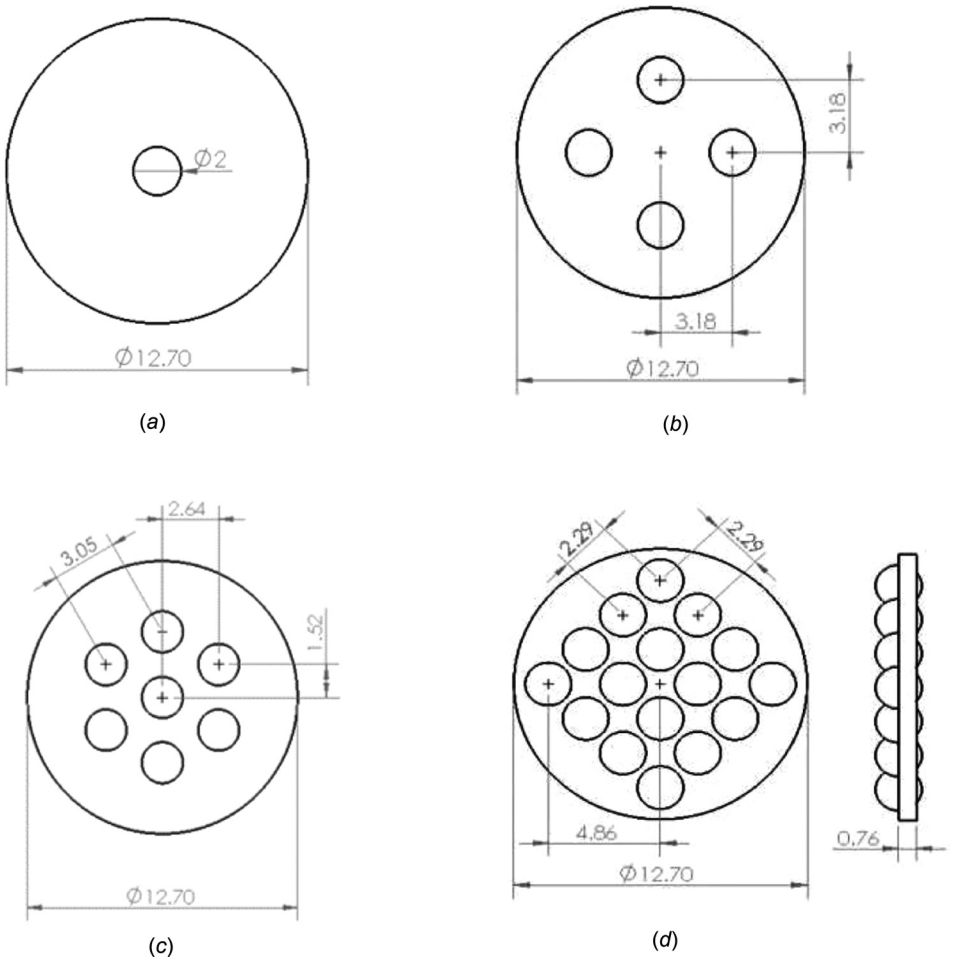

Fig. 3 Particle arrays tested with dimensions in mm. Particles held by a plastic holder unless indicated (*a*) Single particle for tests Oct14-1, Feb15-1, and Feb15-2. (*b*) Four particle diamond used for Feb14-3 (no particle holder). (*c*) Seven particle ring used for Oct14-2. (*d*) Four-by-four grid of 16 particles used for Oct14-3. Side view showing the plastic holder included.

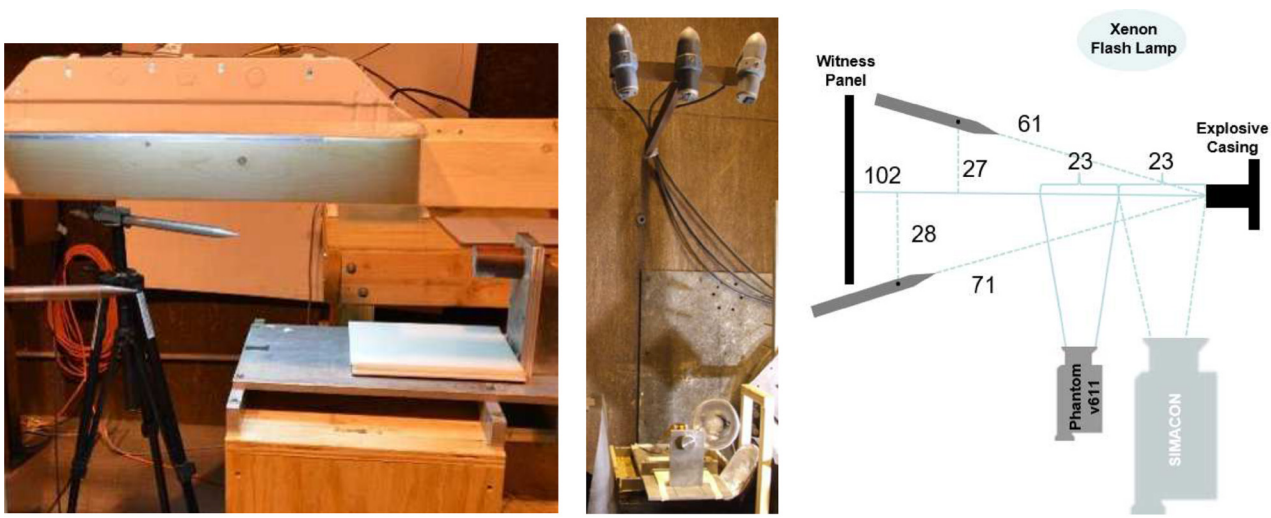

Fig. 4 The experimental setup for those tests conducted in October 2014. (*a*) Photograph of the side view with pressure probes, LED flash lamp, and witness panel clearly visible, (*b*) Photograph from the front view showing X-ray heads above the explosive casing, (*c*) Schematic of the top view with X-ray heads removed for clarity (dimensions in cm).

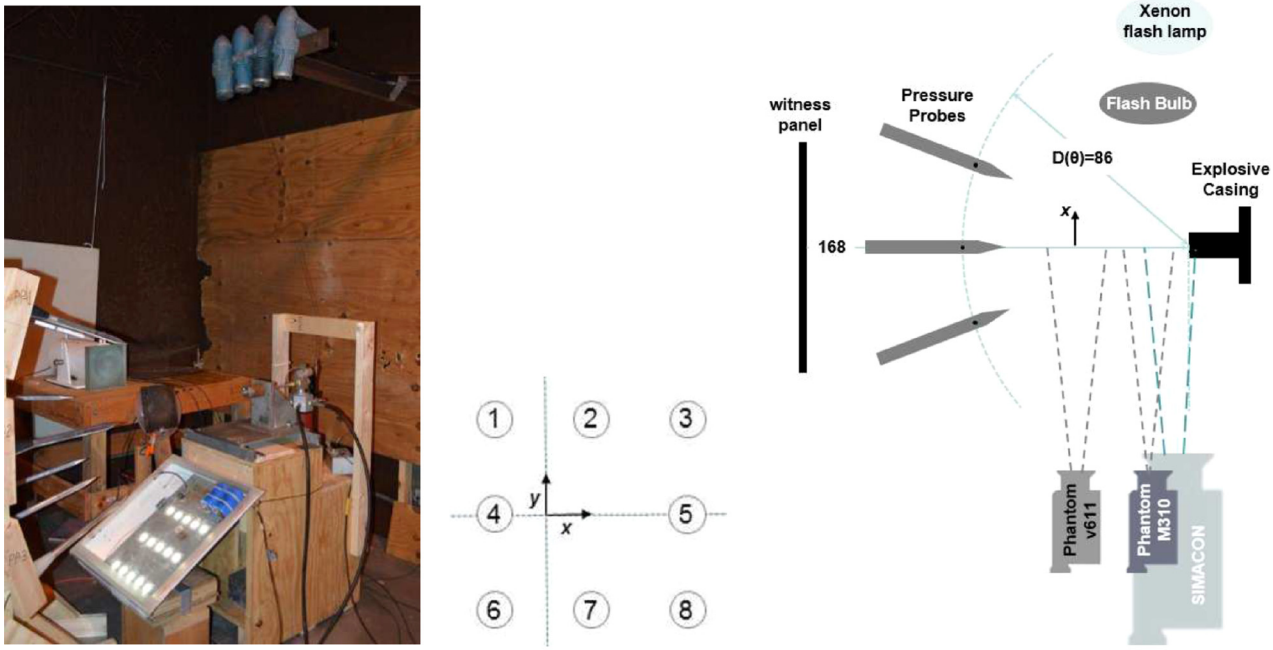

(*a*) (*b*) (*c*)

Fig. 5 The experimental setup for those tests conducted in February 2015. (*a*) Photograph of the side view with pressure probes, LED flash lamp, and X-ray heads clearly visible, (*b*) pressure probe numbering as if looking out the barrel of the explosive casing and the origin placed on the shot line, and (*c*) schematic of the top view with X-ray heads removed for clarity (dimensions in cm).

Table 2 Nominal location of the pressure probes in Cartesian coordinates using the numbering convention shown in Fig. 5(*b*) and the origin at the initial particle location

Probe	x (cm)	y (cm)	z (cm)
1	−12.1	29.8	−80.1
2	14.6	30.2	−79.6
3	42.5	30.5	−68.7
4	−12.1	0.0	−85.5
5	45.7	0.0	−73.3
6	−12.1	−30.5	−79.9
7	14.0	−30.5	−79.6
8	42.5	−30.5	−68.7

Table 3 Frame rates of the February 2015 tests

Test #	Frame Rate (kHz)	Resolution (pix)
Feb15-1	15	512 × 384
Feb15-2	35	320 × 240
Feb15-3	77	256 × 128

Fig. 6 Postshot photograph of the Feb15-2 test article showing significant fragmentation and deformation. The other test articles showed similar damage.

result was confirmed by the Anderson-Darling and the χ^2 goodness-of-fit tests with the same significance level. Attempts to fit the particle diameter with the next two distributions that have a minimum log likelihood, the extreme value and logistic distributions, were also rejected by the Anderson–Darling, Lilliefors, and χ^2 goodness-of-fit with 95% confidence.

Several particles were randomly selected to be measured multiple times, rotating the particles to measure various diameters. The diameter results were within the uncertainty of the micrometer, demonstrating the particles were highly spherical. In addition, to determine if there is a bias due to the user of the micrometers, two users measured each of the particles in a random order using the same micrometer. A table of summary statistics may be found in Table 4. The results show a slight difference in the mean diameter but are within close agreement.

4.2 Particle Density. The results of the particle density were the most surprising of the measured inputs. The particle material was reported to be tungsten in preliminary reports and a nominal density of 19.3 g/cm^3 was expected. However, significant departures from this expected value warranted further investigation,

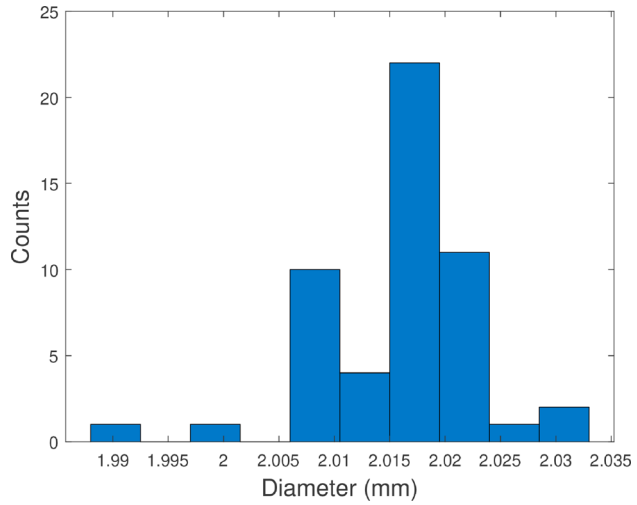

Fig. 7 Distribution of measured particle diameter obtained from a representative sample of 52 particles. A distribution was not successfully fit to the data.

Table 4 Summary statistics for the two testers with the same micrometer

User	μ (mm)	σ (mm)	COV (%)
User 1 (Hughes)	2.016	0.008	0.370
User 2 (Spath)	2.021	0.007	0.321

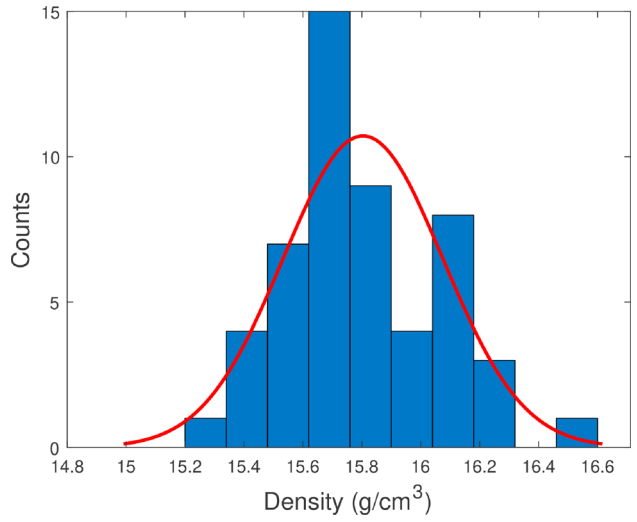

Fig. 8 Distribution of the calculated particle density obtained from the individual method. A normal distribution is fit to the empirical data (solid red line).

hence the presentation of two measurement techniques. First, the density of each individual particle was estimated. Second, the mean density of the particles was confirmed with a fluid-displacement method.

In the first method, the mass of each particle was measured using a mass balance. As the particles were highly spherical, see Sec. 4.1, the volume of the particle was calculated from the measured diameter and the equation of a sphere. A histogram of the particle density results appears to follow a normal distribution, see Fig. 8. The Shapiro–Wilks test with 95% confidence was unable to reject the null hypothesis of normality, returning a p-value of 0.36. The mean and standard deviation of the individual method are reported in Table 5.

Table 5 Summary statistics for the two methods to obtain the particle density

Method	μ (g/cm^3)	σ (g/cm^3)	COV (%)
Individual	15.80	0.07	0.443
Fluid displacement	15.54	0.25	1.59

To confirm the results from the individual measurements above, a Quantachrome UltraPyc 1000 Gas Pycnometer was used to obtain the mean density of the provided tungsten spheres. The pycnometer requires a significant volume of particles in order to accurately measure the volume. All 52 spheres were therefore used, and the reported results are the mean density of the sample. Twelve runs were conducted to reduce the sampling uncertainty of the pycnometer. The results are presented in Table 5. A possible explanation for the discrepancy is that the material was mistakenly reported as tungsten when it is in fact an alloy. The particles were attracted to a magnet suggesting a significant iron content.

4.3 Explosive Length, Diameter, and Density. The explosive pellets were pressed pellets of PBXN-5. While it was not possible for the authors to independently verify the length, diameter, and density of the explosive pellets, internal data from the pellet manufacturer were provided for 26 pellets. The manufacturer-provided data recorded the pellets mass and dimensions from two workers forming the pellets in a pneumatic press. Nominally, the pellets were 12.7 mm diameter with 12.7 mm length. Histograms of the explosive length and density are plotted in Fig. 9. The mold of the press yielded a constant diameter of 12.79 mm. Statistical analysis of the manufacturer-provided data yields a mean length of 12.70 mm with a standard deviation of 0.05 mm.

The literature was consulted for the nominal density of PBXN-5 and a value of 1.762 g/cm^3 was reported [27]. Comparatively, the representative sample yielded a mean of 1.796 g/cm^3 with a standard deviation of 0.003 g/cm^3. The provided data include results from two different workers. As is shown in the histograms of Fig. 9, sufficient differences in pellet manufacture between the two workers were present to give rise to an apparent bimodal histogram in the explosive length and density. To confirm the departure from normality, the Shapiro–Wilks test was performed with 95% confidence and the hypothesis of population normality was rejected for both length and density (p-value of 0.0419 for pellet length and p-value of 0.0316 for pellet density).

4.4 Casing Dimensions. The particle driver is a mild steel casing machined to a 50.4 mm outer diameter with a 13.0 mm central bore. While the geometry was not measured a priori, machining of these materials may easily yield $\pm$0.3 mm tolerance for features of these sizes [28]. The experimentalists confirm checking the casing dimensions before testing and that they conformed closely to dimensions shown in design drawings.

4.5 Particle Initial Location. Images of the experimental setup were processed to check the departure of the particles from nominal. For those tests using plastic holders, configurations 1 and 2 in the experimental setup, the particles were located within 0.25 mm of their nominal values. The photograph of the test article assembly in Fig. 2(*d*) was processed to demonstrate this assertion. The particle is nominally on the centerline of the test setup. Three points were chosen on the circumference of the casing to define a circle with its associated center. The center point of the particle was manually selected. The distance from the center of the circle to the particle center was determined to be 0.22 mm.

More complicated is to determine the degree of departure from nominal values for the four-particle case where no plastic holder was used (i.e., configuration 3). Similar image analysis to that

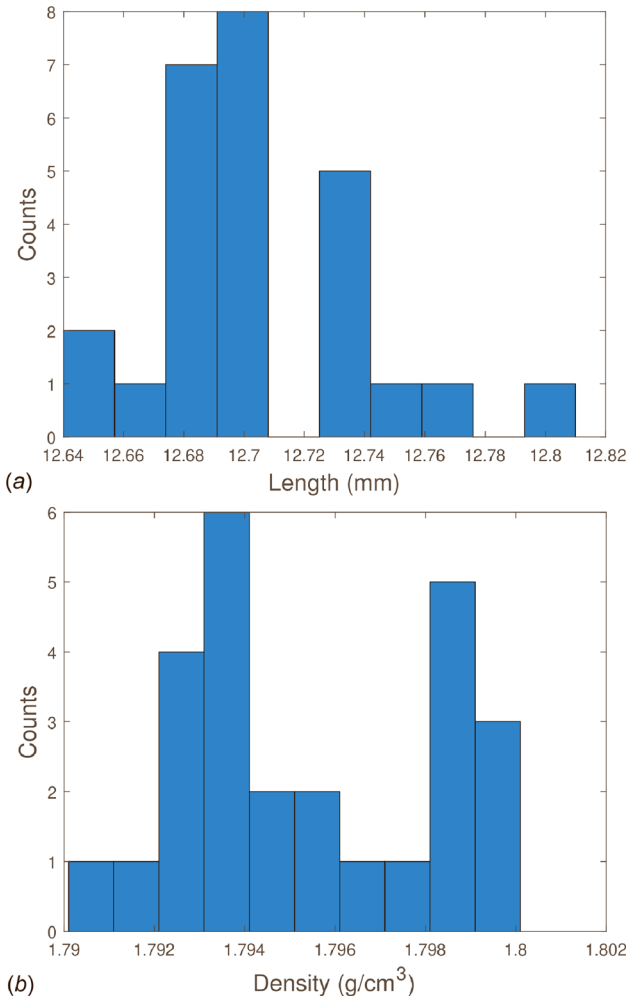

Fig. 9 Provided manufacturer data for PBXN-5 pellets for (*a*) the explosive length and (*b*) the explosive density. The data exhibit a bimodal distribution that is explainable by differences in worker-to-worker variability.

described above for Fig. 2(*d*) was repeated on Fig. 2(*f*) and the results are presented in Fig. 10. The captured particle initial locations are tabulated in Table 6 using the centerline as the origin. Particle numbers correspond to those indicated in Fig. 10. Note the departure of the four particle positions was discovered as a result of forensic investigation.

4.6 Ambient Conditions. Ambient temperature and pressure were not directly measured within the test chamber. In addition, the test chamber is not climate controlled. Ambient conditions varied over the course of the test day. Pressure and temperature bounds were obtained from a weather archival website, Weather Underground, that reported the temperature and pressure for the reported test dates at Eglin Air Force Base, FL and are tabulated in Table 7.

4.7 Measured Inputs Summary—Investigation Findings. The results from Secs. 4.1–4.6 are summarized in Table 8. Results are compared to the initial knowledge at the beginning of the investigation. While in most cases the departure from the mean value is small, some significant departures are evident, such as the particle density. Quantification of the variability of each value is also presented as plus or minus three standard deviations, representing 99.7% confidence intervals for parameters with normal distributions. The particle diameter results are summarized from the micrometer results from the user with greater variability to maintain conservative estimates. Particle density results are from

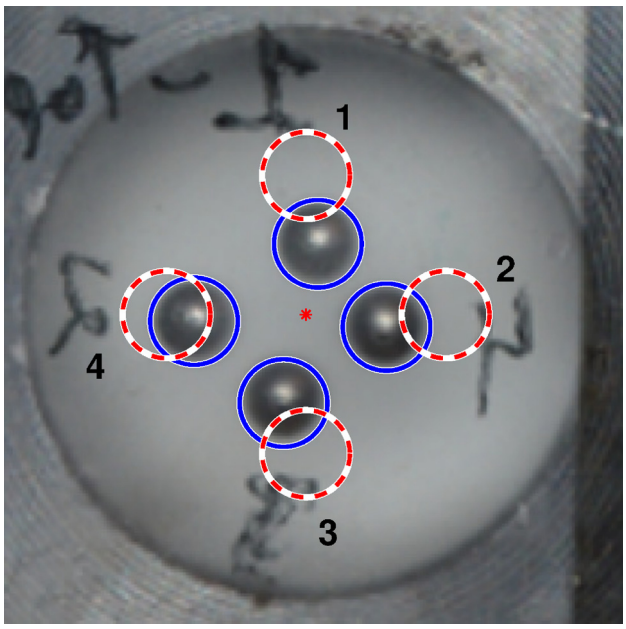

Fig. 10 Departure of the four particle case from nominal values. The actual position of the particles (solid circle) is contrasted to the reported locations (dashed circle). The star shows the location of the bore centerline.

Table 6 Initial particle locations obtained from image analysis with the total distance from nominal location recorded

Particle	Initial location (mm)	Departure (mm)
1	[0.17 1.62]	1.49
2	[1.74 −0.33]	1.46
3	[−0.63 −1.97]	1.42
4	[−2.67 −0.22]	0.52

Table 7 Ambient temperature and pressure bounds within the test chamber for reported test dates

Test dates	Pressure (kPa)	Temperature (°C)
Oct. 22–29, 2014	[101.63 101.93]	[15.4 26.1]
Feb. 26, 2015	[101.35 101.90]	[4.7 8.2]

the individual method. The forensic result in initial particle location is presented as an interval to reflect the large biases present.

5 Experimental Results

This section will present the shock time of arrival, the particle position, the contact front location, transverse shock location, and the trajectory of the particle as processed from the raw data.

5.1 Shock Time of Arrival. The initial time, t_0, for the pressure probes is obtained from the trigger signal to the detonator. Examination of the digital oscilloscope records establishes t_0 within 2 μs. The shock time of arrival (TOA) was estimated by choosing the time t at which the pressure first exceeds 50% of the peak pressure, P_{peak}.

$$\text{TOA} = t(P = 0.5P_{\text{peak}}) - t_0 \tag{1}$$

The reader should note that the pressure probes were at different radial locations for the October 2014 set of data while the February 2015 tests were at the same nominal radial distance from the

Table 8 Investigation findings with regard to uncertain inputs with comparison to initial knowledge

Parameter	Initial knowledge	Forensic result	Method
Particle diameter	2 mm	2.02 ± 0.02 mm	Micrometer—user 1
Particle density*	19 g/cm^3	15.8 ± 0.2 g/cm^3	Derived—individual
Explosive length	38.1 mm	38.1 ± 0.5 mm	Manufacturer data
Explosive diameter*	12.7 mm	12.79 ± 0.00 mm	Manufacturer data
Explosive density*	1.762 g/cm^3	1.796 ± 0.009 g/cm^3	Manufacturer data
Casing dimensions	Nominal	±0.254 mm	Literature [28]
Initial particle location (w/ plastic holder)	Nominal	±0.25 mm	Image analysis
Initial particle location (w/o plastic holder)*	Nominal	[−1.59 −0.52] mm	Image analysis
Ambient pressure (Oct. 22–29, 2014)*	—	[101.63 101.93] kPa	Archival weather
Ambient temperature (Oct. 22–29, 2014)*	—	[15.4 26.1]°C	Archival weather
Ambient pressure (Feb. 26, 2015)*	—	[101.35 101.90] kPa	Archival weather
Ambient temperature (Feb. 26, 2015)*	—	[4.7 8.2]°C	Archival weather

Note: Significant departures from initial knowledge are marked with an asterisk.

initial location of the particle. To remove the effect of the varying probe distances and ambient conditions, the TOA was normalized by the time for an acoustic wave to propagate the same distance

$$a = \sqrt{\gamma R T_{\text{amb}}} \tag{2}$$

$$t^* = \frac{\text{TOA}}{L} a \tag{3}$$

where a is the ambient speed of sound, γ is the ratio of specific heats, R is the specific gas constant, t^* is the normalized shock TOA, L is the distance from the pressure transducer to the particle initial location, and T_{amb} is the mean ambient temperature. Normalized shock time of arrival t^* for all shots is plotted in Fig. 11. The uncertainty in the normalized shock time of arrival is small and so is omitted from the plot for clarity. In Fig. 11, there is an order in which the probes see the shock pass for the February 15 tests. A correlation analysis for the February 15 tests was performed with regard to the x–y location of the probes and the shock time of arrival, and it was found that about 31% of the variation in the shock time of arrival may be explained by the y-location of the probe while only 11% is attributable to the x-location of the probes.

5.2 Particle Position. Due to the optically opaque explosive products, X-rays are necessary to pierce the cloud of explosive products to track the particle. However, these X-rays have some constraints. Each X-ray head produces a single exposure at a set

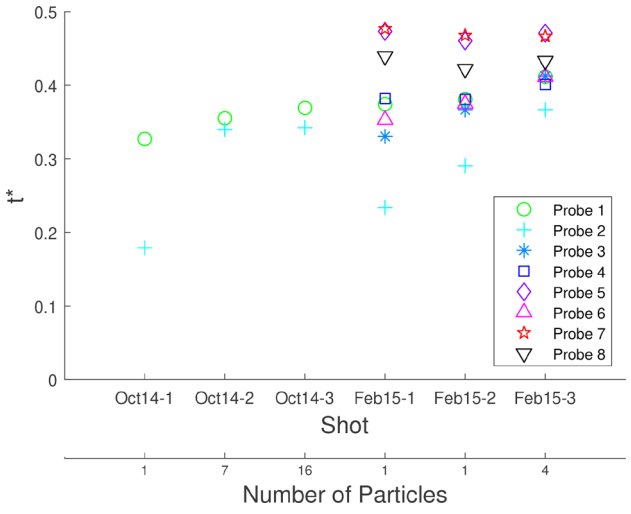

Fig. 11 Normalized shock time of arrival (t^*) for all six tests. Note that a discernible order exists to which probes experience the shock.

delay. The number of X-ray heads was limited to be three or four. In addition, each X-ray head exposes the same film, which causes additional challenges when processing the data. The X-ray heads may also malfunction, reducing the number of data points obtained. Despite these challenges, care was taken to extract accurate position information.

Figure 12 outlines the general steps taken to obtain position information from the X-rays. First, an X-ray of the unexploded driver is examined, Fig. 12(*a*). The explosive casing is known to be 50.4 mm in diameter. Therefore, a calibration constant to convert image distances from pixels to physical units may be obtained for each X-ray head based on this known dimension. Note that there is a thin outer casing around the explosive casing, leading to the slight step visible. Next, the center of the particles is selected, shown as circles in Fig. 12(*b*). Third, the particle origin is found by the average of the top and bottom corners of the casing (indicated by squares in the figure). The origin is not obtained from the calibration image as the X-ray films translate a small but appreciable amount when being exchanged. Finally, the particle position is obtained by finding the distance between the particles, shown as circles, and the origins, shown as triangles, shown in Fig. 12(*c*). For the multiple particle cases where significant spread of the particles is observed, the minimum and maximum particle trajectory is presented for clarity.

The experimentalists documented the times at which the X-ray heads were triggered using a Rogowski coil wrapped around the trigger lines, with the resulting voltage recorded by a digital oscilloscope. A sample digital oscilloscope record is shown in Fig. 13. The nominal time at which the X-ray was to trigger is 110 μs in this case. The Rogowski coils produce a voltage proportional to the time rate of change of the current within the trigger line. Due to the derivative nature of the recorded signal, the record is quite noisy. The uncertainty is only partially alleviated by integration due to lack of knowledge of how closely the X-ray heads trigger toward the peak voltage. The real X-ray exposure time is closer to 113 μs with a conservative standard deviation of 1 μs to encapsulate the uncertain nature of where the X-ray head fires. This process may then be repeated for each X-ray exposure.

The extracted particle positions are shown in Fig. 14(*a*). The error bars for the data are mostly occluded by the data markers. As discussed above, the horizontal error bars are obtained from examination of the digital oscilloscope records. The horizontal error bars are one standard deviation of the timing uncertainty, very close to 1 μs for most X-ray timings. The vertical error bars are obtained from the standard deviation of a Monte Carlo approach to measure the dependence on user selections in the image processing results. Each X-ray image was processed three times and the mean and standard deviation of the particle position calculated. Markers represent mean values and vertical error bars are one standard deviation and are on the order 0.1 mm. Note the four-particle case did not exhibit any appreciable spread and the results are presented as a single trajectory.

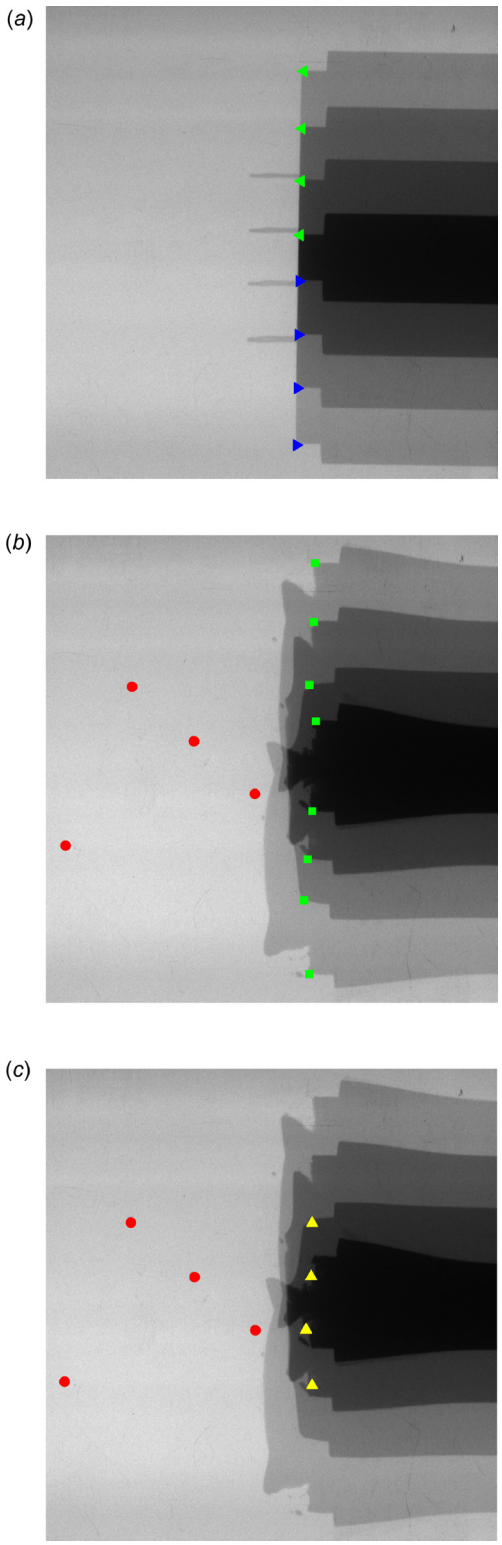

Fig. 12 Three-step process for calculating the position from the multiple exposure X-rays: (*a*) obtain a calibration constant for each X-ray head, (*b*) select particles and casing edges, and (*c*) obtain the physical distance the particle has traveled from the origin

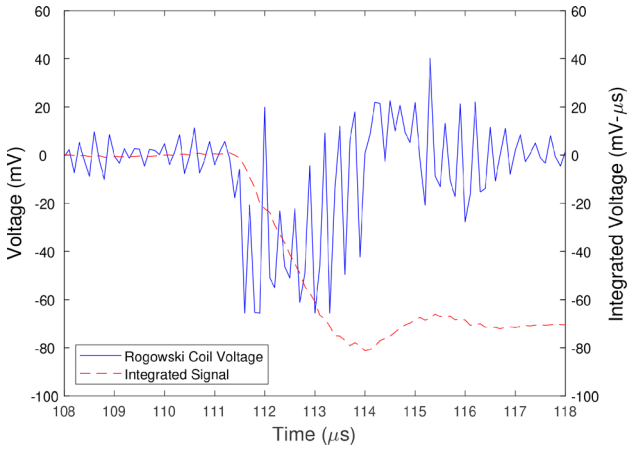

Fig. 13 Digital oscilloscope record of the X-ray head trigger for the October 14-1 test, sampled at 10 MHz. Voltage measured by the Rogowski coils is proportional to the time rate of change of current within the trigger line while the integrated voltage is proportional to the current within the trigger line.

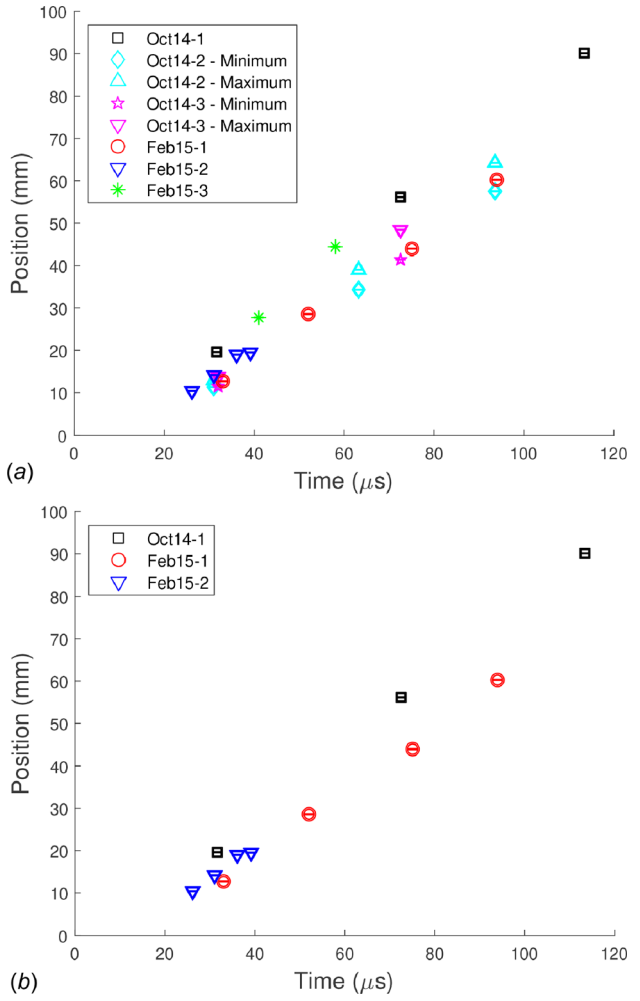

Fig. 14 Particle position obtained from X-ray images: (*a*) aggregate results for all six shots and (*b*) plot of only the single particle shots to show the difference between the two test configurations

The multiple particle shots, Oct14-2 and Oct14-3, exhibit minimum particle trajectories that track closely with the single particle results of Feb15-1 and Feb15-2. The maximum trajectories begin to show some acceleration due to neighboring particles. The two tests that depart from the general trend, Oct14-1 and Feb15-3, are those two loading configurations that differed from the rest of the tests. Without the forensic investigation, these results would seem to be subject to larger shot-to-shot variability than is present.

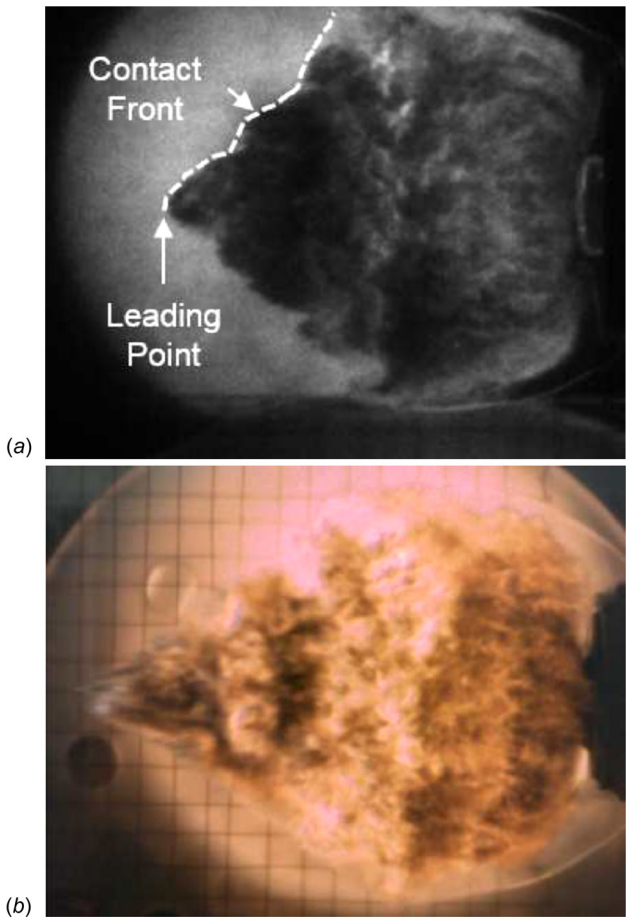

Fig. 15 Sample images from the single particle test, Feb15-1: (*a*) Example SIMACON image showing the explosive products clearly 25.5 μs following the detonation trigger. Note the bright circle in the background is due to the xenon flash lamp. (*b*) Example Phantom M310 image 40 μs following the detonation trigger. Flow is from right to left.

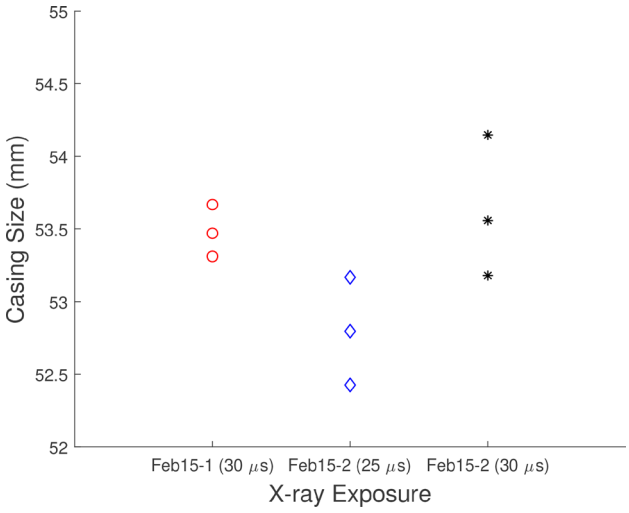

Fig. 16 Casing size measurements from X-ray exposures. Multiple points show the variability in casing size dependent on user selection in the image processing scheme. Close agreement between the casing size at 30 μs allows use of the casing size at 25 μs to calibrate the SIMACON images during the dynamic event.

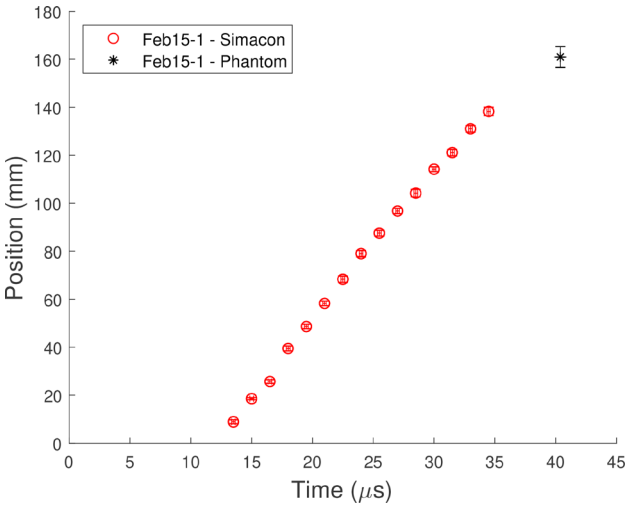

Fig. 17 Contact front location results. Contact front results are obtained from selection of the leading point of the cloud of explosive products. Extrapolation of the Simacon results show close agreement, after calibration from the deformed casing with the Phantom camera results.

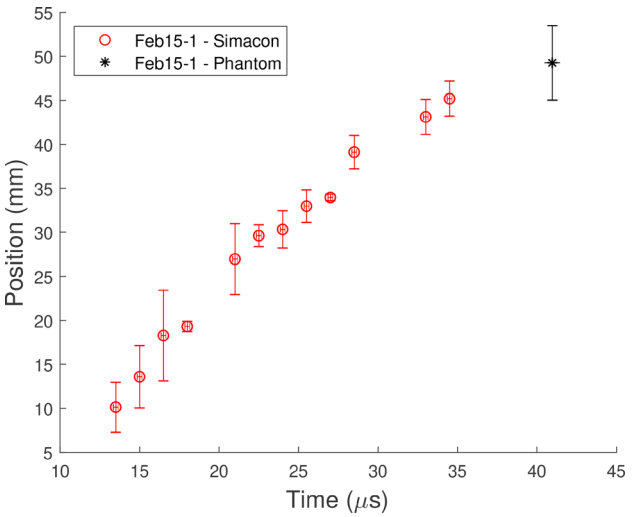

Fig. 18 Transverse shock location results. Shock locations are chosen parallel to the explosive casing face.

The single particle shots are plotted together to show the degree which the repeated tests disagree (see Fig. 14(*b*)). Relatively close agreement between the single particle cases of the same configuration is obtained for the repeated single particle cases, February 15-1 and February 15-2. However, the large departure of the single particle case, October 14-1, is due to the containment effect of the barrel.

5.3 Contact Front Location. The contact front location is one of only two metrics that provides information of the behavior of the gas at early times. The explosive products are easily observable in both the SIMACON and the Phantom images collected (see Fig. 15) and form a sharp conical structure. Contact front location results were obtained by selection of the farthest point of the contact front (the point of the sharp cone). The Phantom cameras (v611 and M310) collected only a few images in which the propagating explosive front is visible due to their relatively low frame rate. In addition, the Phantom v611 cameras were located

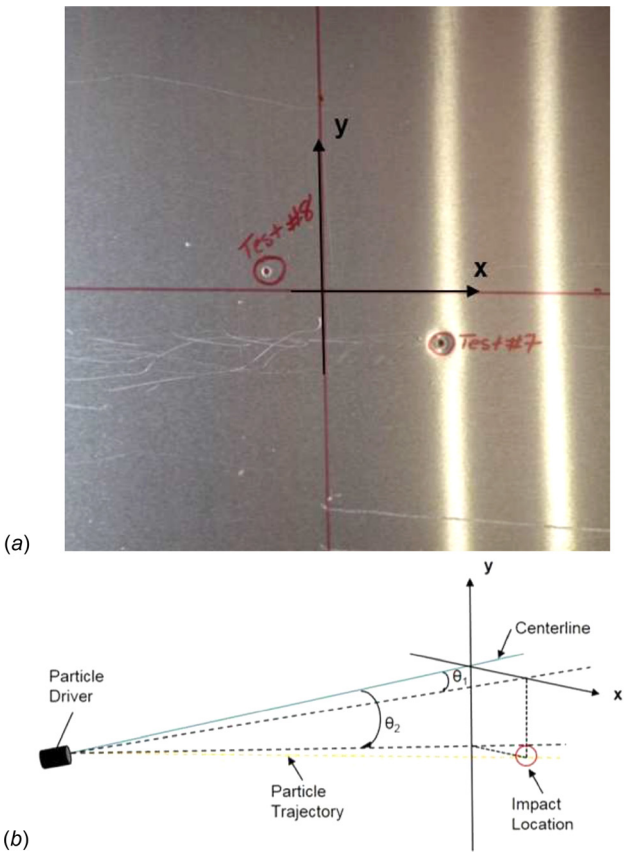

Fig. 19 Witness panel angles and results. (*a*) Particle impact locations for the repeated test of a single particle (Feb15-1 is labeled "Test #7" and Feb15-2 is labeled "Test #8"). (*b*) Angle conventions for witness panel impact locations.

away from the explosive casing and only calibrated within the field of view. The exact location of the field of view with respect to the explosive casing is not known. The Phantom v611 camera data are therefore of little use and are not presented here. These serious deficiencies reduce the number of contact front locations from the Phantom cameras to a single data point.

The SIMACON images also suffer from a lack of a reliable calibration and additional steps were required to calibrate the images. Only a single data set was usable, February 15-1, but still two major calibration challenges were present in obtaining contact front location from the SIMACON images. First, the dark SIMACON images before the explosion lack the ability to locate and calibrate off the casing. Second, the SIMACON images may be calibrated from the dynamic images, but significant deformation of the casing occurs. To overcome these obstacles, additional information from the X-ray images concerning the casing size during the dynamic event is necessary. However, the SIMACON image where the casing is clearly visible does not have a corresponding X-ray exposure. The closet match is the 25 μs exposure of the February 15-2 test. The size of the explosive casing is obtained from X-ray exposures in the February 15-1 and February 15-2 tests, with three user selections of the casing for each exposure, and plotted in Fig. 16. The close agreement in casing sizes at 30 μs between the February 15-1 and February 15-2 tests allow use of the casing size from the February 15-2, 25 μs X-ray exposure. The casing size uncertainty is then propagated through the processing of the SIMACON image and represented as vertical error bars (bars are one standard deviation). The timing uncertainty of the SIMACON comes from the exposure times of the frames, 0.3 μs for the February 15-1 tests. Contact front results are plotted in Fig. 17. The SIMACON and Phantom cameras demonstrate close agreement despite the additional calibration steps.

Table 9 Final particle position and trajectory angles for the February 2015 shots

Test	x, y (mm)	θ_1(deg)	θ_2(deg)
February 15-1	(46, −19)	−1.57	−0.65
February 15-2	(−21, 7)	0.72	0.24
February 15-3	(84, 182)	−2.87	6.20
	(−192, −148)	6.53	−5.05

Note: Two of the particles in the four-particle case did not impact the aluminum panel.

5.4 Transverse Shock Location. The second metric that provides information on the early time gas behavior is the transverse shock location. The shock preceding the contact front normal to the casing is not visible. However, the shock traveling parallel to the casing face is visible in both the SIMACON and the Phantom images collected (see Fig. 15). Following the same calibration and feature extraction procedure discussed in Sec. 5.3, the transverse shock location results are shown in Fig. 18. As before, the casing size uncertainty is propagated through the processing of the SIMACON image. However, the shock exhibits significantly less contrast than the contact front and the uncertainty of the shock location was significantly greater. The timing uncertainty of the SIMACON images is 0.3 μs.

5.5 Final Particle Location. Thin, aluminum witness panels were used to determine the particles' impact points with a fixed plane in the far-field (i.e., 168 cm from the initial location). The crosshair in Fig. 19(*a*) marks the test article's centerline, and was determined with a bore sighting laser. Figure 19(*a*) shows results for the witness panel for the February 15-1 and February 15-2 tests. Witness panel data are unavailable for the October 14 tests. Witness panel data were processed to provide average angles at which the particle moves over the 168 cm to impact. The angle θ_2 provides some measure of the out-of-plane component of the position not captured by the X-ray images. The angle conventions used are provided in Fig. 19(*b*). The angles obtained are tabulated in Table 9. However, the reader will note that two of the particles were not recovered for February 15-3, indicating that for at least two of the particles, out-of-plane motion is significant.

6 Conclusions

Forensic uncertainty quantification is a focused investigation of past experiments to fill gaps in knowledge to bring an experiment up to validation quality. FUQ involves an investigator, preferably an independent third party, who carefully defines the scope of their investigation. The investigator collects all available "crime scene" documentation of the experimental setup and corresponds with the experimentalist as their "primary witness." In addition, the investigator carefully performs experiments in their "forensics laboratory" to quantify uncertain inputs or recreate aspects of the experiment. By performing FUQ, the investigator reduces the uncertainty of the experiment sufficiently that the experimental results will be of greater value to development of models. Without FUQ, an overly conservative estimate for uncertainty will have to be adopted when faced with an uncertain input. The overly conservative uncertainty estimate results in large propagated uncertainty in the corresponding model. Forensic investigation of the experiments assigns realistic uncertainty bounds to uncertain inputs and removes bias by improving knowledge of experiment details. The propagated uncertainty is smaller as a result of more constrained inputs. Smaller uncertainties allow useful failure to guide model development.

The idea of FUQ is used in analyzing experiments that comprise of six explosive tests involving the explosive dispersal of metal particles. Three single particle shots were repeated, followed by three tests with arrays of particles. The scope of the investigation was defined by our motivation for the experimental

Table 10 Table of two major FUQ investigation findings for each aspect of the experiments: experimental setup, uncertain inputs, and uncertain outputs

	Finding 1	Finding 2
Experimental setup	Additional loading configuration identified not recalled by the experimentalists	Explosive position within the casing differed from design documentation
Uncertain inputs	Particle density is significantly lower than tungsten, likely a ferrous alloy	Large departures from nominal particle position for 4-particle case
Uncertain outputs	High-speed imagery was not calibrated sufficiently with respect to casing in most cases	Particle position results showed low shot variability when corrected for configuration

results: extension of the particle-drag model to the high Mach and Reynolds number regime of detonation. The details of the experiments were reconstructed based on documentation, photographs, and corroboration with experimentalists. A surprising result for the experimental setup involved the discovery of a loading configuration not reported by the experimentalist. In fact, its existence had to be proved by the investigator. The uncertain inputs were then carefully identified and their uncertainty quantified through testing of representative samples in the laboratory. Many inputs had statistically significant departures from nominal values but relatively small variabilities. The largest departure from initial knowledge was the particle density. A summary table of uncertain inputs is reported in Table 8. Finally, the experimental results were processed from the raw data paying attention to the precision of the detonator trigger signal, quantification of timing uncertainty, and quantification of position uncertainty. Interpretation of the particle position data was aided by FUQ by identification of testing configurations that differed from the majority of tests. Those tests with differing configurations may be discarded as they demonstrate significantly different results. Table 10 presents some of the highlights from the investigation for each aspect of the experiments.

The above efforts have allowed accurate quantification of gas motion resulting from an initial detonation and simultaneous particle motion driven by the rapidly expanding gas. Results on the following three quantities along with their uncertainties are presented: (i) the location of the transverse air shock as a function of time, (ii) the front location of the contact surface between the products of detonation and air as a function of time and (iii) the time-dependent position of metal particles driven by the explosion. These results are intended to serve as a benchmark for the development and testing of drag models that are appropriate under detonation conditions and for validation of future simulations.

Acknowledgment

The authors would like to acknowledge the efforts of Myles Delcambre of AFRL for conducting the October 2014 experiments presented in this paper and making the results available for use. The authors would like to thank Shirly Spath for her assistance in measuring particle diameters. This work was supported by the U.S. Department of Energy, National Nuclear Security Administration, Advanced Simulation and Computing Program, as a Cooperative Agreement under the Predictive Science Academic Alliance Program, under Contract No. DE-NA0002378.

Funding Data

- U.S. Department of Energy (Funder ID: 10.13039/100000015).
- National Nuclear Security Administration (Funder ID: 10.13039/100006168).

Nomenclature

a = ambient speed of sound
L = distance from initial particle location to the pressure probe
P_{peak} = peak pressure measured by the pressure probes
R = specific gas constant
R_p = radius of the particle
t_0 = pressure probe initial time
t^* = normalized shock time of arrival
T_{amb} = ambient temperature
TOA = shock time of arrival
u_s = shock speed
γ = ratio of specific heats
μ = sample mean
σ = unbiased sample standard deviation

References

[1] Crowe, C., Schwarzkopf, J., Sommerfeld, M., and Tsuji, Y., 2011, *Multiphase Flows With Droplets and Particles*, 2nd ed., CRC Press, Boca Raton, FL.
[2] Loth, E., 2008, "Compressibility and Rarefaction Effects on Drag of a Spherical Particle," AIAA J., **46**(9), pp. 2219–2228.
[3] Parmar, M., Haselbacher, A., and Balachandar, S., 2010, "Improved Drag Correlation for Spheres and Application to Shock-Tube Experiments," AIAA J., **48**(6), pp. 1273–1276.
[4] Clift, R., and Gauvin, W. H., 1970, "The Motion of Particles in Turbulent Gas Streams," Proc. Chemeca'70, **1**, pp. 14–28.
[5] Bailey, A., and Starr, R., 1976, "Sphere Drag at Transonic Speeds and High Reynolds Numbers," AIAA J., **14**(11), p. 1631.
[6] Jourdan, G., Houas, L., Igra, O., Estivalezes, J.-L., Devals, C., and Meshkov, E., 2007, "Drag Coefficient of a Sphere in a Non-Stationary Flow: New Results," Proc. R. Soc. A Math. Phys. Eng. Sci., **463**(2088), pp. 3323–3345.
[7] Hughes, K., Diggs, A., Littrell, D., Balachandar, S., Haftka, R. T., Kim, N. H., Park, C., and DelCambre, M., 2017, "Uncertainty Quantification of Experiments on a Small Number of Explosively-Driven Particles," AIAA Paper No. 2017-1463.
[8] Ling, Y., Haselbacher, A., and Balachandar, S., 2011, "Importance of Unsteady Contributions to Force and Heating for Particles in Compressible Flow—Part 1: Modeling and Analysis for Shock-Particle Interaction," Int. J. Muhiphase Flow, **37**(9), pp. 1026–1044.
[9] Ling, Y., Haselbacher, A., and Balachandar, S., 2011, "Importance of Unsteady Contributions to Force and Heating for Particles in Compressible Flows—Part 2: Application to Particle Dispersal by Blast Waves," Int. J. Multiph. Flow, **37**(9), pp. 1013–1025.
[10] Sun, M., Saito, T., Takayama, K., and Tanno, H., 2005, "Unsteady Drag on a Sphere by Shock Wave Loading," Shock Waves, **14**(1–2), pp. 3–9.
[11] Tanno, H., Itoh, K., Saito, T., Abe, A., and Takayama, K., 2003, "Interaction of a Shock With a Sphere Suspended in a Vertical Shock Tube," Shock Waves, **13**(3), pp. 91–200.
[12] Tanno, H., Komuro, T., Takahashi, M., Takayama, K., Ojima, H., and Onaya, S., 2004, "Unsteady Force Measurement Technique in Shock Tubes," Rev. Sci. Instrum., **75**(2), pp. 532–536.
[13] Bredin, M., and Skews, B., 2007, "Drag Measurement in Unsteady Compressible Flow—Part 1: An Unsteady Flow Facility and Stress Wave Drag Balance," RD J. South Afr. Inst. Mech. Eng., **23**(1), pp. 1–10.
[14] Parmar, M., Haselbacher, A., and Balachandar, S., 2009, "Modeling of the Unsteady Force for Shock-Particle Interaction," Shock Waves, **19**(4), pp. 317–329.
[15] Britan, A., Elperin, T., Igra, O., and Jiang, J., 1995, "Acceleration of a Sphere Behind Planar Shock Waves," Exp. Fluids, **20**(2), pp. 84–90.
[16] Wagner, J. L., Beresh, S. J., Kearney, S. P., Pruett, B. O. M., and Wright, E. K., 2012, "Shock Tube Investigation of Quasi-Steady Drag in Shock-Particle Interactions," Phys. Fluids, **24**(12), p. 123031.
[17] Bordoloi, A. D., Martinez, A. A., and Prestridge, K., 2017, "Relaxation Drag History of Shock Accelerated Microparticles," J. Fluid Mech., **823**, p. R4.
[18] Zhang, F., Frost, D., Thibault, P., and Murray, S., 2001, "Explosive Dispersal of Solid Particles," Shock Waves, **10**(6), pp. 431–443.
[19] Frost, D. L., Zarei, Z., and Zhang, F., 2005, "Instability of Combustion Products Interface From Detonation of Heterogeneous Explosives," Int. Colloq. Dyn. Explos. React. Syst., pp. 1–6.
[20] Frost, D. L., Ornthanalai, C., Zarei, Z., Tanguay, V., and Zhang, F., 2007, "Particle Momentum Effects From the Detonation of Heterogeneous Explosives," J. Appl. Phys., **101**(11), p. 113529.

[21] Frost, D. L., Grégoire, Y., Petel, O., Goroshin, S., and Zhang, F., 2012, "Particle Jet Formation During Explosive Dispersal of Solid Particles," Phys. Fluids, **24**(9), p. 091109.
[22] Maxey, M. R., and Riley, J. J., 1983, "Equation of Motion for a Small Rigid Sphere in a Nonuniform Flow," Phys. Fluids, **26**(4), p. 883.
[23] Gatignol, R., 1983, "The Faxén Formulas for a Rigid Particle in an Unsteady Non-Uniform Stokes-Flow," J. Méc. Théor. Appl., **2**(2), pp. 143–160.
[24] Parmar, M., Haselbacher, A., and Balachandar, S., 2011, "Generalized Basset-Boussinesq-Oseen Equation for Unsteady Forces on a Sphere in a Compressible Flow," Phys. Rev. Lett., **106**(8), pp. 2–5.
[25] Parmar, M., Haselbacher, A., and Balachandar, S., 2012, "Equation of Motion for a Sphere in Non-Uniform Compressible Flows," J. Fluid Mech., **699**(5), pp. 352–375.
[26] Annamalai, S., and Balachandar, S., 2017, "Faxén Form of Time-Domain Force on a Sphere in Unsteady Spatially Varying Viscous Compressible Flows," J. Fluid Mech., **816**, pp. 381–411.
[27] Dobratz, B., and Crawford, P., 1985, *LLNL Explosives Handbook - Properties of Chemical Explosives and Explosive Stimulants*, Livermore, CA.
[28] Groover, M., 1999, *Fundamentals of Modern Manufacturing: Materials, Processes, and Systems*, Wiley, New York.